IJCRT.ORG ISSN : 2320-2882

INTERNATIONAL JOURNAL OF CREATIVE RESEARCH THOUGHTS (IJCRT)

An International Open Access, Peer-reviewed, Refereed Journal

OPTOELECTRONIC PROPERTIES OF FABRICATED $BaPbCe_2O_7$ NANOPARTICLES FOR PHOTOCATALYTIC BREAKDOWN OF MALACHITE GREEN: A GREENER APPROACH

[1]Tejveer Singh Tanwer, [2]Jinesh Menaria, [3]Dushyant Kumar Prajapati, [4]Jeevan Kunwar Chouhan and [5]Shipra Bhardwaj

[1, 2, 3, 4, 5]Department of Chemistry, Government Meera Girls College, Mohan Lal Sukhadia University, Udaipur, Rajasthan, India.

Abstract: The synthesis of a novel nanoparticle $BaPbCe_2O_7$, utilizing co-precipitation method is carried under controlled conditions. Structural and morphological properties of the as synthesized material are meticulously characterized through various analytical techniques like X-ray diffraction (XRD), field-emission scanning electron microscopy (FE-SEM) etc. Furthermore, we investigated the impact of calcination temperature on the morphology of the nanomaterial. UV–Vis spectroscopy revealed a peak absorbance at 192 nm, with an optical bandgap estimated to be 2.32 eV. Subsequently, the synthesized nanoparticles (NPs) are then employed as catalyst for the photodegradation of malachite green (MG) dye. A systematic kinetic investigation is conducted to extract maximum degradation conditions. Remarkably, $BaPbCe_2O_7$ exhibited significant degradation efficiency, achieving approximately 89% degradation within a 20 minute time frame. Optimal degradation performance was attained at pH 10.0, catalyst dosage of 0.18 g, initial dye concentration of 1.4×10^{-4} moles/Litre accompanied by a light intensity of 1960 mW/cm^2. Moreover, we assessed the recyclability of the photocatalyst up to five cycles with negligible loss in weight and efficiency. These findings underscore the potential of $BaPbCe_2O_7$ nanoparticles as promising photocatalyst for the treatment of water contaminated with specific concern to organic dye.

Keywords: Photocatalysis, Photodegradation, Coprecipitation, Dye degradation, Water treatment.

1. Introduction

The direct discharge of hazardous organic contaminants from textile industries into water bodies poses a serious environmental concern worldwide [1, 2]. Among these contaminants, textile dyes constitute a significant portion of organic pollutants and even a minor release of these dyes can severely impact both human health and aquatic ecosystems [1–3]. One such dye is malachite green which is a triphenylmethane basic dye, readily soluble in water that possesses antimicrobial properties [4], used to dye silk, cotton, leather, wool and paper and it is also employed as a fungicide and disinfectant in the fish farming industry [5]. Malachite green is environmentally persistent and acutely toxic to a wide range of aquatic and terrestrial animals. Also it is highly cytotoxic to mammalian cells [6]. This dye is characterized by a complex molecular structure, high stability, non-biodegradability and high resistance to light and oxidizing agents [4]. In recent nanotechnology breakthroughs, metal oxide nanoparticles (NPs) have become crucial for various

technological applications, including sensors, photocatalysis, antibacterial treatments, anticancer therapies, energy storage and environmental remediation [7]. Among different metal oxide NPs, titanium dioxide (TiO_2), tin dioxide (SnO_2), zinc oxide (ZnO), copper oxide (CuO) and barium oxide (BaO) have been extensively studied for their potential in environmental and biomedical applications [8,9]. BaO NPs, with distinct characteristics such as a highly reactive surface, a broad bandgap, narrow

emission and strong electrical conductivity, find applications in crown glass production, humidity sensors and photocatalysis, in medical and pharmaceutical fields, diagnostic imaging, orthopedic medicines, in-vitro apoptosis and DNA damage studies [10,11,12]. Furthermore, BaO NPs are attractive candidates for efficient photocatalytic applications due to their high surface-to-volume ratio, superior oxygen adsorption capability, wide availability and cost-effectiveness [13]. Metal and metal oxide nanoparticles are commonly used in the industrial applications because of having optical, electronic, mechanical, magnetic, biomedical, sensory and catalytic properties [14, 15]. Lead oxide (PbO) is recognized as an important industrial material that can be used in batteries, composite electrode, optical sensor, reusable catalyst and glass industry [16, 17]. In addition, the band gap changes according to the lead-oxygen ratio. Special attention is paid to PbO nanostructures due to its photoconductive properties [18]. Lead oxide, particularly in nanoparticle form (PbO NPs), has shown promising photocatalytic activity due to its unique properties, including its bandgap and ability to absorb light. Taking advantage of their inherent photocatalytic capabilities, such nanoparticles are capable of initiating and enhancing degradation reactions when exposed to light, thus providing a sustainable and energy-efficient strategy for treating wastewater. CeO_2 is another semiconductor photocatalyst with various applications. However, its band gap is in the wide range of 2.6 to 3.4 eV, depending on the preparation method [19, 20]. Furthermore, CeO_2 exhibits promising photocatalytic activity. Nonetheless, the position of CB and VB limits its application as an efficient photocatalyst utilizing solar energy, even though CeO_2 can absorb a larger fraction of the solar spectrum [21]. The main properties that make CeO_2 significant as a photocatalyst and photoelectrode material applied in the degradation of various pollutants result from its high band gap energy, high refractive index, high optical transparency in the visible region, high oxygen storage capacity, and chemical reactivity [22, 23]. In light of the promising features of quaternary photocatalysts and their vital role in advanced oxidation processes (AOPs), here we report the synthesis, detailed characterization and application of a novel quaternary photocatalyst, $BaPbCe_2O_7$ aimed at efficient dye removal from wastewater systems. The synthesized nanoparticles were characterized in the accepted manuscript aspects of crystallinity, morphology, purity, compositional analysis and optical properties via various spectroscopic and analytical techniques. The outcomes of fabrication, characterization and its photocatalytic performance evaluation are elaborately addressed and discussed in further sections.

II. Experimental

2.1 Materials and Method

Barium nitrate, lead nitrate and cerous nitrate (sourced from Merck) were used as precursor materials in the synthesis of the photocatalyst, while sodium hydroxide from CDH was employed as the precipitating agent. Malachite green functioned as the model pollutant in the study. To adjust the pH of the solutions, hydrochloric acid (CDH) and sodium hydroxide (CDH) were utilized, with pH measurements conducted using a pH meter (Hena imported pen type). UV-Vis spectrophotometry (CHINO) was employed for kinetic study to record the optical density of solutions at various time intervals. For irradiation, a 200Watt tungsten lamp (Philips) was utilized and light intensity was measured using a solarimeter (New CHEM Dt 1307). Scavengers, namely Isopropanol, EDTA, KI and ammonium oxalate were incorporated to trap active species. All chemicals were utilized in their LR grade, with a purity range of approximately 95-99%.

For kinetic study, solution of malachite green dye (MG) was taken in a borosil beaker, pH was measured and photocatalyst was added. It was then exposed to light and after certain time intervals, optical density (OD) was recorded. A plot of log optical density (O.D.) verses time was straight line suggesting that the reaction of degradation follows pseudo first order kinetic law.

2.2 Instrumentation:

The many techniques used to characterize the produced $BaPbCe_2O_7$ photocatalyst are covered in detail here. A Panalytical X Pert Pro X-ray diffractometer was used to record the X-ray diffraction (XRD) pattern using Ni-filtered Cu Ka radiation at 10 kV and 80 mA for monochromatized Cu Ka (k = 1.5418 Å) radiation, with a scan range of 10\2h\80. A Nova Nano FE-SEM 450 (FEI) scanning electron microscope was used to perform scanning electron microscopy (SEM) measurements in order to examine the surface roughness and morphology of the samples. Using energy dispersive X-ray, SEM imaging conditions were analyzed for composition. Physical Electronics performed the XPS spectra (Model: PHI 5000 VersaProbe III analysis). Using a Perkin Elmer FT-IR Spectrum 2 spectrophotometer, Fourier transform infrared (FT-IR) spectra of KBr pellets in the 400–4000 cm-1 range were captured. Using a UV-vis NIR spectrophotometer (Perkin Elmer, U.S.A.), UV-vis diffuse reflectance spectra (DRS) were measured. A high-resolution transmission electron microscope was employed to monitor the observations using the HRTEM Hitachi H-7500.

The absorbance of the dye was measured using a UV–Vis spectrophotometer (CHINO). Using the following formula, the degradation percentage of the dye was calculated:

$$\% \text{ degradation} = (C_o - C/C_o) \times 100$$

Where C_o and C represent the initial concentration and final concentration of the dye at different time intervals, respectively.

III. Results and Discussion

Synthesis of $BaPbCe_2O_7$ nanoparticles:

A solid co-precipitation method was employed for synthesis of $BaPbCe_2O_7$ and controlled conditions were maintained during the process. 0.1 M solutions of each barium nitrate, lead nitrate and cerous nitrate were prepared and pH was recorded as 6.5, 3.8 and 3.1 respectively. All the three solutions were mixed to attain the pH 4.3. The mixture was stirred for 2 hours and while stirring, 5N NaOH solution was added drop by drop for precipitation to obtain yellow colored material. This was then stirred for half an hour and then allowed to settle down. Temperature during the process was maintained at 25°C. Supernatant liquid was checked for further precipitation, filtered and dried in a microwave oven at 100°C. Yellow solid was obtained with yield 45.56 g and the yield percentage was 91.8 %. This was then subjected to calcination at 500°C for 2 hours. The color of the prepared solid changed to black with yield of 33.23 g and the yield percentage was 73 %.

Characterization:

The EDS spectrum of $BaPbCe_2O_7$ NPs confirms the synthesis of $BaPbCe_2O_7$ NPs as Ba, Pb, Ce and O were observed with elemental weight percentages of 13.73, 20.72, 26.62 and 11.2 respectively. X ray diffraction analysis (XRD) proved it to be nano crystalline material with average crystal size to of 58.12 nm. X-ray Photoelectron Spectroscopy (XPS) spectrum of the synthesized nanomaterial revealed distinct peaks at 880.6 and 897.3 eV corresponding to Ce (II) 3d 5/2 and Ce (II) 3d 3/2, suggesting cerium ions in oxidation states of +2 and +4. UV–Vis spectroscopy revealed the optical band gap to be 2.32 eV. Details are discussed here:

3.1 X-ray Diffraction Analysis (XRD analysis):

XRD data were used to study the crystal structure and phase identification. The graphic figure 1 displays the $BaPbCe_2O_7$ nanocomposite's XRD pattern and table 1 contains the data for calculation of crystal size. The (111), (200), (220) and (311) planes of $BaPbCe_2O_7$ are represented by the XRD peaks, which are situated at angles (2θ) = 28.47, 32.97, 47.38 and 56.44 respectively. The standard XRD peaks of BaO, PbO and CeO_2 showed a high association with them [24, 25, 26]. The quaternary metal oxide nano powder $BaPbCe_2O_7$ reveals that the minimal crystallite size is indicated by the growth peak intensity and drop in the FWHM. The corresponding nanomaterials' lattice parameters, degree of crystallinity, lattice strain and crystallite size were computed. The photocatalyst appears to be extremely crystalline in nature, based on the crisp and moderately strong intense diffraction facets. That was recorded using a powder diffractometer [27, 28]. A considerable increase in crystallinity at a higher calcination temperature is suggested by the improved resolution and intensity of the diffraction peaks at 500 °C. The interaction between the BaO, PbO_2 and CeO_2 phases may be the cause of the nanocomposite's slight peak deviation. The material's nanocrystalline nature is shown by peak broadening in diffraction spectra, which may be the consequence of hydroxide growth in the composites. The nano photocatalyst's diffraction pattern exhibits a sharp and powerful peak at 2θ = 28.47, which is ascribed to the (111) plane and its associated interplanar distance (d) of 0.31 nm.

Scherer's method $D=0.9\lambda/\beta \cos\theta$ was used to calculate the crystallite size of the produced samples from the X-ray diffraction data. In this formula, λ represents the wavelength of the X-rays (1.5418), β is the FWHE of the peak with the highest intensity, and θ is the diffraction angle. The Debye-Scherrer formula is used to

determine the average crystallite size of pure nanoparticles and Bragg's law was used to determine that the nanoparticles from the high intense peak (28.4°) in the XRD spectra of $BaPbCe_2O_7$ [29]. Based on calculations on the enlargement of the diffraction peaks in the XRD patterns, the crystallite size (DXRD) of pure $BaPbCe_2O_7$ nano powder, calcined at 500 °C, is 58.12 nm on average [30, 31].

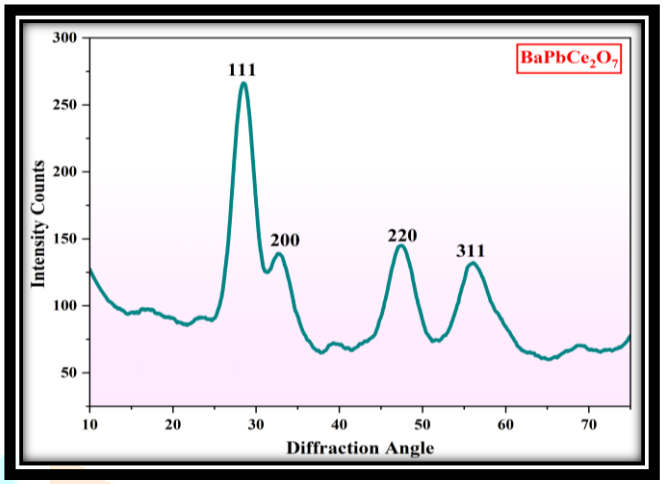

Figure 1: XRD pattern of $BaPbCe_2O_7$ photocatalyst

Table 1: Crystal size calculation for $BaPbCe_2O_7$

Peak No.	Angle 2θ	FWHM	Crystallite size (nm)	Average crystal size (nm)
1	28.47	0.1775	49.76	58.12
2	32.97	0.1525	60.93	
3	47.38	0.1354	67.28	
4	56.44	0.1644	54.52	

3.2 Field Emission Scanning Electron Microscopic Analysis (FESEM):

SEM morphology photos of the $BaPbCe_2O_7$ nano catalyst describe the surface morphology, particle size, and size distribution of the produced particles. An EDX (model Nova Nano FE-SEM 450 (FEI)) and a field-emission scanning electron microscope (FESEM) equipped with an accelerating voltage of 15 kV (TLD-SE) was used to analyze the form and consistency of the nanoparticles. The FESEM images captured after a 4-hour annealing procedure at 500 °C are displayed in figure 2. It can be inferred that the substance is made up of agglomerated, porous, and uniformly distributed nanoparticles. The spherical cubic shape and restricted size distribution of the nanocomposite have been observed. The rough, cubic particles with irregular orientation were also visible due to the nanocomposite's surface form. Because of the interaction between three different types of oxides, which changed the kinetics and shape of the generated particles, the nanocomposite was found to have a considerable agglomeration orthorhombic crystal. The average particle size is 58.01 nm as determined and dispersed. The crystallite size computed using Scherer's formula is similar to the particle size as indicated by the SEM result.

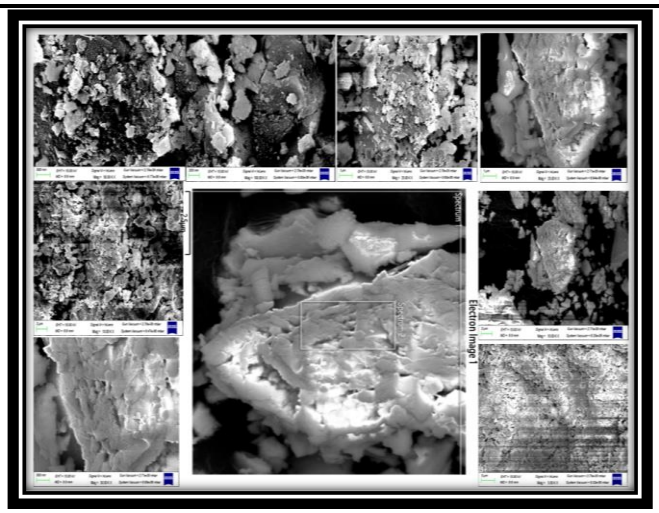

Figure 2: FESEM images of $BaPbCe_2O_7$ photocatalyst

3.3 Energy Dispersive X-ray Spectroscopic analysis (EDX analysis, Elemental composition study):

The elemental composition and purity of the generated quaternary perovskites were further confirmed. Figure 3 displays the metal oxides' and the produced $BaPbCe_2O_7$ nanoparticles' energy dispersive x-ray spectroscopy (EDX) spectra and validates the fabrication of $BaPbCe_2O_7$ nanoparticles. It shows a prominent band for Ba, Ce, Pb and O with elemental weight percents of 13.73, 26.62, 20.72, and 22.72, respectively. According to the study, every element has a unique atomic structure, which results in a unique collection of peaks in the electromagnetic emission spectrum. Based on the peak strength, the necessary elements were present in the following ratios: 1.0:1.0:1.9:7.0 for Ba, Pb, Ce and O. The figures accord well with the suggested formula, $BaPbCe_2O_7$. The weight percentage and atomic percentage of the elements present in the photocatalyst are shown in table 2.

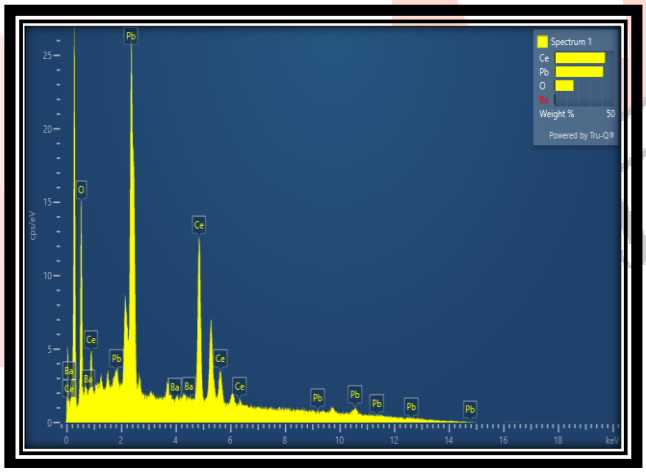

Figure 3: EDX Spectra with elemental mapping of $BaPbCe_2O_7$ nanoparticle

Table 2: Elements present in $BaPbCe_2O_7$ photocatalyst

Element	Weight%	Atomic%
Ba	13.73	18.6
Ce	26.62	38.03
Pb	20.72	28.12
O	11.2	15.2
Totals	100.00	100.00

3.4 Fourier Transform Infrared Spectroscopy (FTIR):

FT-IR measurements were made in order to determine the presence of functional groups on the NPs' surface. The FTIR spectroscopic analysis was carried out between the frequency range of 400 and 4000 cm^{-1} using a Perkin Elmer spectrometer. The details are given in figure 4. According to the study, the synthesized

photocatalyst seems to be crystalline and nano powder-like. The IR spectral peaks of the first oxide have been shown to change when another oxide is present. O-H bond bending and stretching vibrations, which may be brought on by adsorbed water molecules, also produce certain peaks at higher wavelengths. 3741.34, 3333.33, 2704.16, 2350.83, 2050.23, 1985.06, 1746.98, 1295.59, 1039.04, 810.33, 770.18, 711.03 and 678.96 cm^{-1} are the main peaks observed. Metal-oxygen stretching is usually attributed to bands in the 600–1000 cm^{-1} range, while metal–oxygen bending vibrations are linked to bands in the 600–800 cm^{-1} range. The OH bending of water molecules adsorbed on the composite's surface (O-H bending and stretching vibrations) is responsible for the band at 1295.59 cm^{-1}, whereas surface hydroxyl is responsible for the peaks at 3333.33 cm^{-1} and 1746.98 cm^{-1} [33].

Adsorbed atmospheric CO_2 stretching vibration and C–O stretching is responsible for the maxima at 2350.83 and 1039.04 cm^{-1}. The bending mode (stretching and bending vibrations) of the BaO and PbO bond is responsible for the peak at 810.33 and 678.96 cm^{-1}, which indicates the primary absorption band [32,39,33,35]. The band (stretching and bending vibrations) mode of the CeO_2 bond, which involves motion of a change in CeO_2 bond length, is responsible for the absorption band at 678.96, 770.18, and 711.03 cm^{-1}. Therefore, the existence of both peaks indicates that the sample contains a strong metal–oxygen link [11,13,14,38]. The CeO_2 component can be attributed to the peak seen at 1053 cm^{-1}. CeO_2 stretching vibration is the cause of the frequencies in the 900 cm^{-1} to 820 cm^{-1} range [30]. There has been a noticeable change in the overall peaks. All of the sharp peaks indicate strong stretching vibrations, ruling out the existence of pollutants. The analysis found that coprecipitation, which is used throughout the synthesis process, has a considerable impact on the photocatalytic performance. In accordance with the XRD data, these bands validate the creation of a cluster structure and are associated with the environment around the $BaPbCe_2O_7$. The FT-IR analysis solely shows nanoparticles formed during the chosen chemical process, as there are no additional functional peaks associated with secondary products [24,25].

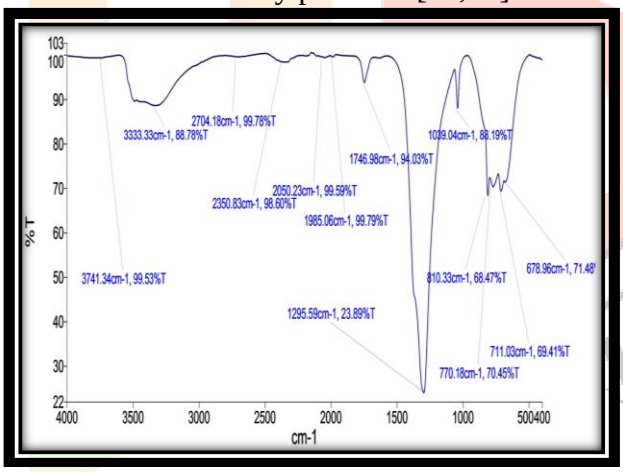

Figure 4: FTIR spectra of $BaPbCe_2O_7$ photocatalyst

3.5 X-Ray Photoelectron Spectroscopy (XPS):

The chemical composition, elemental oxidation states and surface shape of materials, all affect how well they perform in catalytic studies. XPS analysis is used to determine the electrical and chemical states of the produced material as well as the chemical environment of the barium, lead and cerium components. This study is conducted using an XPS instrument (Model: PHI 5000 Versa Probe III analysis) and gives the deconvoluted graphs and displays the XPS 104 spectra data. XPS provided detailed information on the oxidation states on the surface because of its inherent capacity to discriminate between elemental and chemical state information. The primary components found on the surface are revealed by the spectrum displayed in Figure 5 (a) and deconvoluted graphs are presented in figure 5 (b). Examining the transition peaks involving the Ba $3d^5$, Pb 4f, Ce 3d, C 1s and O 1s orbitals allows one to establish the composition of the photocatalyst to be $BaPbCe_2O_7$.

The binding energy peaks of 777.92.1 and 799.4 eV correspond to Ba 3d 5/2 and 3d 3/2 transitions, in the composite. This implies that Ba is present in the +2 oxidation state. [40, 41, 42]. Pb (II) (4f 7/2 and 4f 5/2) was identified by the binding energy peaks at 136.7 and 141.47 eV and are clearly observed in deconvoluted spectra. Oxidation state +2 for Pb is confirmed based on these peaks. [20, 21, 22]. Ce (II) 3d 5/2 and Ce (II)

3d 3/2 was identified by the binding energy peaks at 880.6 and 897.3 eV and the oxidation state +4 is assigned to Ce based on these peaks. [47, 48, 46, 24].

These useful explanations demonstrate how an oxygen-rich environment might degenerate into an oxygen-deficient one. The formation of the BaO-PbO-CeO_2 nanocomposite results in bonded oxygen on the surface of nanocrystals, which explains the change in the oxygen environment shown by the signal at 528.02 eV in the XPS of O1s. The generated chemical contains an oxygen bond between three metal cations. Consequently, the O1s spectra show three peaks, which represent no energy differences and Ba-O, Pb-O and Ce-O bonding. Equal intensity confirms the bond between oxygen and three metal cations. The formation of the $BaPbCe_2O_7$ nanocomposite was verified by considering XRD. The close proximity of well-stabilized nanoparticles, as indicated by the XPS measurements, is crucial for the strong photocatalytic activity.

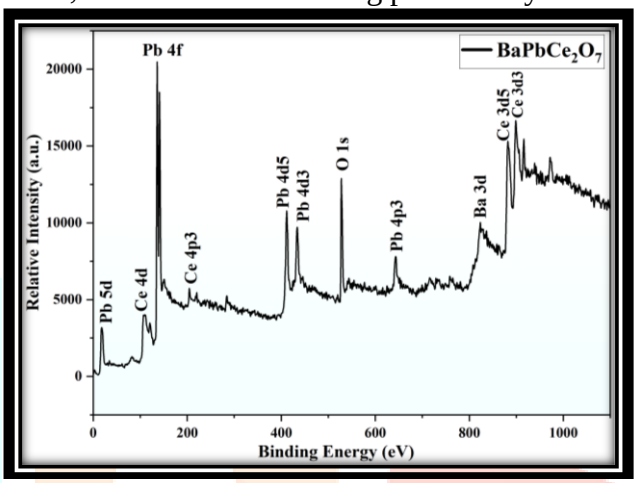

Figure 5 (a)- XPS spectra of $BaPbCe_2O_7$ photocatalyst

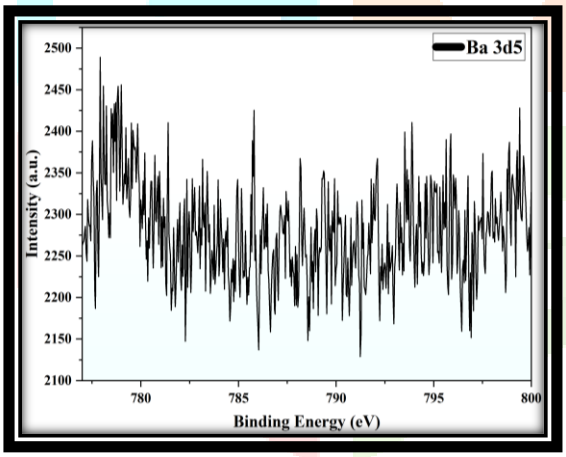

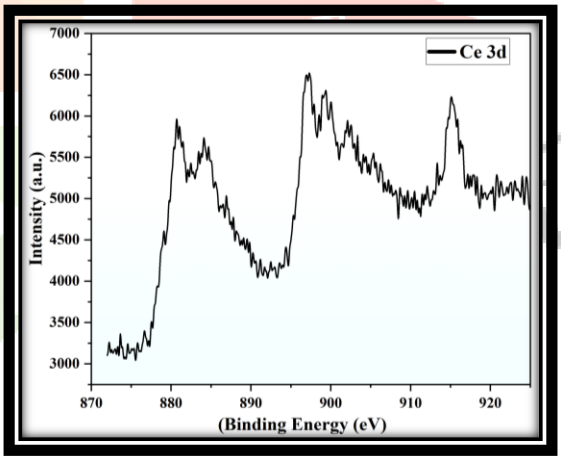

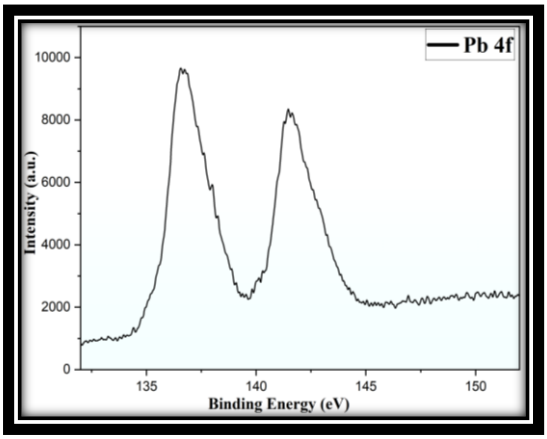

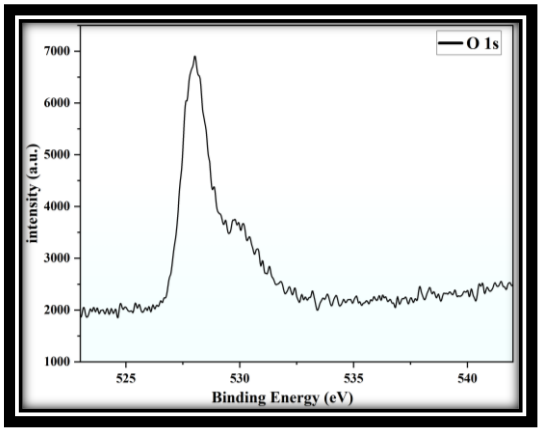

Figure 5: (b) Deconvoluted XPS spectra of individual elements

3.6 UV-VIS NIR Analysis:

The product's UV absorption is correlated with particle size when the crystal nucleus's formation rate exceeds its growth rate; the smaller the particle size, the higher the UV absorption value. The UV-VIS-NIR spectrum was used to measure the optical properties of the generated $BaPbCe_2O_7$ nanoparticles, which is displayed in the figure 6 at wavelengths between 200 and 800 nm. The photocatalytic activity of semiconductor materials is largely explained by their light absorption characteristics. Broad absorption bands at 254, 315, 351 and 464 nm respectively, reflect the BaO, CeO_2 and PbO peaks [26,19,37,31,50,51]. The quantum size effect could be one reason for this. The nanoparticle is smaller than the wavelength of de Broglie. In this scenario, distinct electronic energy levels would arise in all materials due to the spatial confinement of the electrons and holes.

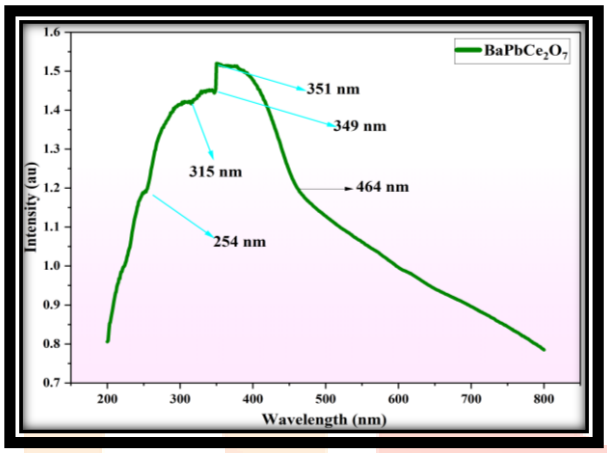

Figure 6: UV-Vis spectra of $BaPbCe_2O_7$ photocatalyst

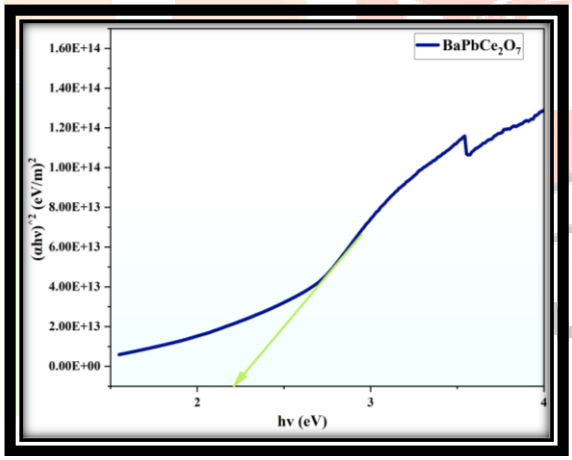

Figure 7: Band gap energy determination of $BaPbCe_2O_7$ photocatalyst by τ (tauc) plot

Semiconductor materials' optical characteristics, which significantly affect their photodegradation performance, are mostly determined by their bandgap energy. The formula [$\alpha = A (h\nu - Eg)/ h\nu$] was used to determine the band gap width associated with the $BaPbCe_2O_7$ composite samples. The findings (figure 7) demonstrated that the creation of composite samples significantly decreased the breadth of the band gap, enhanced the composite samples' capacity to respond to visible light, and enhanced their photocatalytic efficiency [39].

$\alpha = A (h\nu - Eg)/ h\nu$

Eq. is used to determine the absorption coefficient (α). The band gap energy is computed by extending the linear portion of the graph between $(\alpha h\nu)^2$ and photon energy ($h\nu$) until it intersects the x-axis. According to calculations, the Eg value for nanoparticles comes out to be 2.32 eV.

4. Photocatalytic activity of $BaPbCe_2O_7$ nanoparticles:

For the kinetic study, a solution of dyes is taken in a borosilicate beaker, the pH is measured and the photocatalyst is added. It is then exposed to light and after certain time intervals, optical density (O.D.) is recorded. A straight line is observed in the plot of 1+ log of O.D. versus time during the reaction, as shown in

figure 8. Various models, including pseudo-first-order and pseudo-second-order (Type-1, Type-2, Type-3, Type-4 and Type-5), are studied to understand the degradation process. After analyzing the data, it is observed that the pseudo-first-order model best explained the degradation process. The optimized conditions for the breakdown of MG dyes are identified as follows: pH 10.0, 0.18 g of photocatalyst, dye concentration 1.2×10^{-4} M and light intensity 1960 $mWcm^{-2}$. A typical run is given in figure 8.

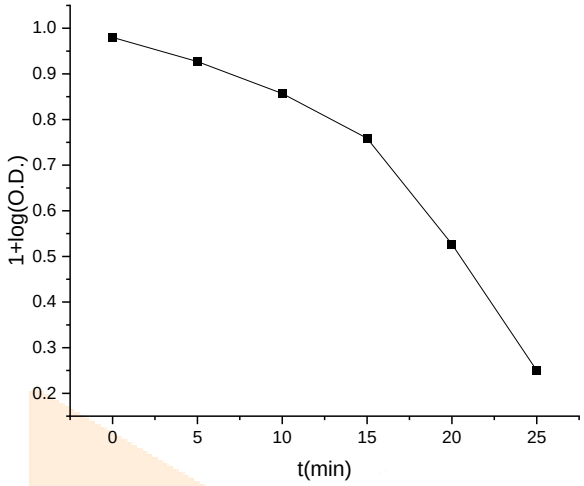

Figure 8. A typical run

4.1 Effect of photocatalyst $BaPbCe_2O_7$ dose:

The impact of the photocatalyst $BaPbCe_2O_7$ dosage on the degradation process is meticulously investigated by varying its weight, while ensuring all other variables remained constant. figure 9 vividly portrays the outcomes of this exploration. Interestingly, the highest degradation rates are observed for MG at a photocatalyst dose of 0.18 g. The rate constants are presented in table 3. This can be attributed to the increased surface area available for absorbing light radiation, thus generating a greater number of electron-hole pairs. Such an outcome is linked to the fact that a higher dosage of the photocatalyst leads to a larger surface area of particles exposed to light. However, upon further increasing the photocatalyst dose, an intriguing observation emerged: the reaction rate began to decline. This phenomenon is attributed to the recombination of electrons and holes, which occurs due to their enhanced quantity at higher photocatalyst doses.

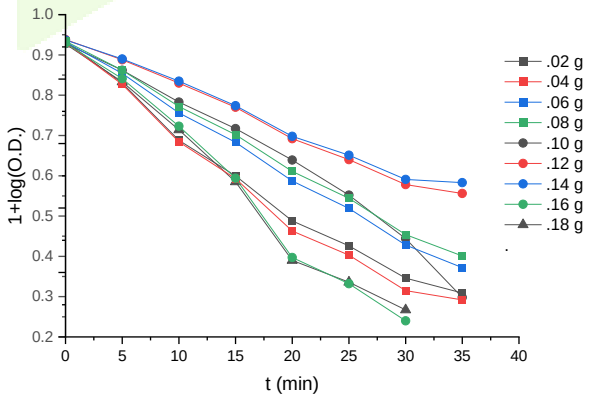

Figure 9. Effect of $BaPbCe_2O_7$ Dosage (g/50mL) on degradation of MG

Table 3: Rate constants at different dose of $BaPbCe_2O_7$ photocatalyst

Doses of $BaPbCe_2O_7$ (g/50mL)	$k \times 10^{-4}$ (Sec^{-1})
0.02	6.41
0.04	5.19
0.06	6.58
0.08	6.71
0.10	6.43
0.12	7.15
0.14	7.33
0.16	7.77
0.18	**8.44**

4.2 Effect of dye concentration:

The study is conducted within the range of 0.4×10^{-4} to 1.8×10^{-4} M of dye concentration, with all other variables held constant. The resulting data for MG dye are illustrated in figure 10 and table 4. Observations indicate that the reaction rate increases with an increase in the concentration of dye. This is because more dye molecules are available to absorb photons from light, becoming excited in the process. However, after reaching a maximum value (at 1.4×10^{-4} M) further increases in dye concentration led to a decrease in the rate of degradation. This decline occurs because beyond a certain concentration, additional dye darkens the color of the reaction mixture and begins to act as a filter to the incident light.

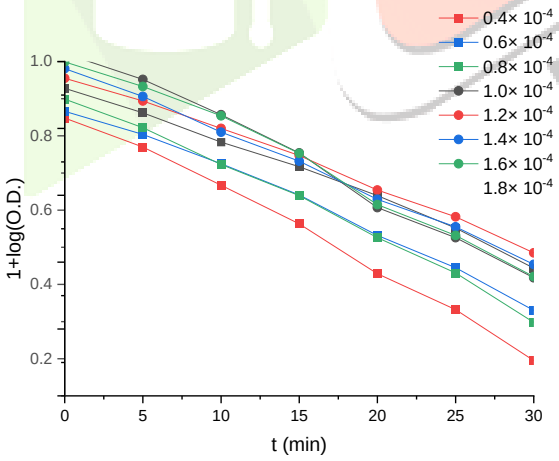

Figure 10. Effect of concentration (moles L^{-1}) of MG on degradation

Table 4: Rate constants at different concentration of MG

MG×10^{-4} (moles L^{-1})	k×10^{-4} (Sec^{-1})
0.4	5.76
0.6	6.05
0.8	4.96
1.0	7.41
1.2	6.38
1.4	**8.44**
1.6	6.57
1.8	5.02

4.3 Effect of intensity of light:

The experiment entailed adjusting the light intensity within the range of 930 to 1960 $mWcm^{-2}$, with corresponding data presented graphically in figures 11 and tabulated in table 5. All other experimental variables are kept constant throughout. It is observed that the rate of photocatalytic degradation increased in tandem with the rise in light intensity. This phenomenon can be attributed to the greater number of photons striking per unit area over time as light intensity escalates. Consequently, there is an increase in the presence of excited dye molecules and electron-hole pairs at the photocatalyst's surface. The peak degradation rate for MG is observed at a light intensity $1960mWcm^{-2}$. Further increase in light intensity was found to cause thermal side reaction and so were not considered for study.

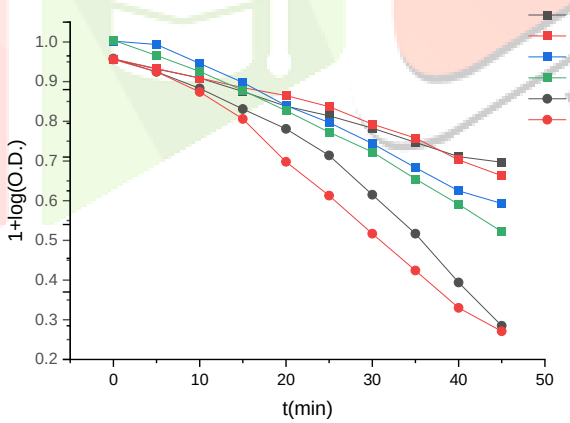

Figure 11. Effect of intensities of light (mW/cm^2) on degradation of MG

Table 5: Rate constants at different intensities of light

Intensity of light ($mWcm^{-2}$)	k × 10^{-4} (Sec^{-1})
1960	**8.44**
1710	4.54
1560	4.66
1390	2.93
1150	3.02
930	2.86

4.4 Effect of pH:

The breakdown speed of the dye changes significantly depending on the pH of the solution because dyes are quite sensitive to pH variations. Some dyes even alter their color when the pH changes. To understand this better, systematic adjustment of the pH of the solution, with keeping all other factors constant, is put in. Interestingly, it is noticed that the initial optical density of the solution changed as the pH varied, as shown in detailed graph. The study focused on the pH range of 6.5 to 10.0 for MG with the results depicted in figure 12 and rate constants are given in table 6. This thorough analysis reveals how crucial pH is in influencing the dye degradation process. The rate of photocatalytic degradation increased as the pH rises. The peak degradation point for MG dye is observed at pH 10.0. Further increase in pH made the solution opaque and interfered in the observations, thus was not carried out. The effect can be explained on the basis that adding base increases the number of OH^- ions which become available to the holes generated at photocatalyst surface causing abstraction of an electron and producing $OH^\bullet$ free radicals. These free radicals attack the weaker double bond site of the dye breaking its conjugation and further breaking it into smaller fragments.

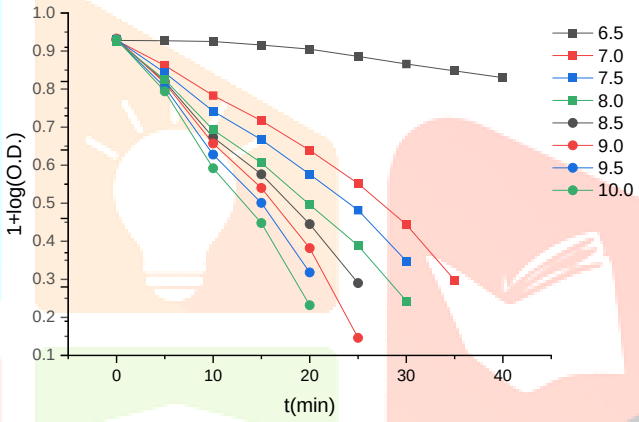

Figure 12. Effect of pH on degradation of MG

Table 6: Rate constants at different pH

pH	k × 10^{-4} (Sec^{-1})
10.0	**8.44**
9.5	7.17
9.0	5.47
8.5	4.19
8.0	3.59
7.5	4.18
7.0	2.54
6.5	2.16
6.0	0.29

The mechanism is given as:

$h\nu$ (photon) + MG → MG^1 (Dye in singlet exited state)

MG^1 → MG^3 (Dye in triplet exited state) (ISC)

$h\nu + BaPbCe_2O_7 \rightarrow h^+ + e^-$

$h^+ + OH^- \rightarrow h + OH^\bullet$

$OH^\bullet + MG^3 \rightarrow$Leuco form of MG → $H_2O + CO_2 + NO_2$ etc. (degraded product)

4.5 Ascertaining the reactive species:

Numerous scavengers are utilized to investigate the involvement of reactive species in degradation reactions. The study of degradation of MG dye using the nanomaterial $BaPbCe_2O_7$ in the presence of 2 ml of scavenger (EDTA, $OH^\bullet$ free radical scavenger) is conducted and is shown in figure 13. Ceasing the reaction suggests that $OH^\bullet$ free radical is the active species causing degradation of MG dye. The degradation stabilized, with only approximately 5% of the dye being degraded.

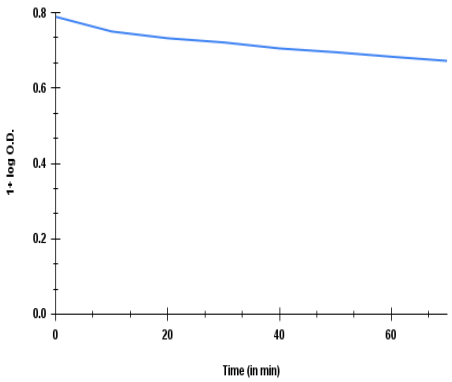

Figure 13- Degradation of malachite green in presence of EDTA

5. Conclusion

In conclusion, it is stated that a novel $BaPbCe_2O_7$ nanocomposite is successfully synthesized using a simple co-precipitation method. The material is thoroughly characterized through various analytical techniques like XRD, EDX, FESEM, UV-Vis etc. The calculated energy band gap of 2.32 eV indicates its strong photocatalytic potential, as it effectively reduces the recombination of photo-generated electron–hole pairs on the surface. The synthesized nanocomposite was applied for solar-light-driven degradation of malachite green into smaller, non-toxic fragments. A systematic kinetic investigation confirmed that the degradation process follows pseudo-first-order kinetics. Scavenger experiments revealed that hydroxyl free radicals play a key role in the reaction mechanism, which was subsequently proposed. Furthermore, recycling studies demonstrated that the nanocomposite can be reused multiple times for wastewater treatment with appreciable efficiency. Over all this work highlights an effective strategy for removing colored pollutants from water, contributing to sustainable water purification for broad applications.

6. Acknowledgement: The authors are thankful to the Materials Research Centre, MNIT Jaipur, Rajasthan, India, SAIF laboratory, Punjab University, Chandigarh, India for carrying out the analysis

REFERENCES

1. Thomas, V. J., Ramaswamy, S. Application of Graphene and Graphene Compounds for Environmental Remediation. *Sci. Adv. Mater.*, **2016**, 8, 477-500.
2. Hu, X., Tian, J., Yang, H., Li, T., Wei, N., Cui, H. Chemical Assembly of Titania P25 on MoO_3 Nanobelts with Enhanced UV and Visible Photocatalytic Activities. *Sci. Adv. Mater.*, **2016**, 8**,** 2313–2321.
3. Rajkumar, D., Kim, J.G. Oxidation of various reactive dyes with in situ electro-generated active chlorine for textile dyeing industry wastewater treatment. *J. Hazard. Mater.*, **2006**, 136, 203- 212.
4. Vergis, B. R., Hari Krishna, R., Kottam, N., Nagabhushanana, M.B., Sharath, R., & Darukaprasad, B. Removal of malachite green from aqueous solution by magnetic $CuFe_2O_4$ nano-adsorbent synthesized by one pot solution combustion method. *J. Nanostruct. Chem.*, **2018**, 8(1), 1–12.
5. Kabeer, F. A., John, N. & Abdulla, M. H. Biodegradation of malachite green by a newly isolated *Bacillus vietnamensis* sp. MSB17 from continental slope of the Eastern Arabian Sea: Enzyme analysis, degradation pathway and toxicity studies. *Bioremediat. J.*, **2019**, 23(4), 334–342.
6. Sutar, S. S., Patil, P.J.,Tamboli, A.S., Patil, D.N., Apine,O.A., & Jadhav, J.P. Biocatalysis and Agricultural Biotechnology Biodegradation and detoxification of malachite green by a newly isolated bioluminescent bacterium *Photobacterium leiognathi* strain MS under RSM optimized culture conditions. *Biocatal. Agric. Biotechnol.*, **2019**, 20, 101183.
7. Linic, S., Aslam, U., Boerigter, C., Morabito. M. Photochemical transformations on plasmonic metal nanoparticles. *Nat. Mate.*, **2015**, 14, 567-576.
8. Muthuvel, A., Jothibas, M., Manoharan. C. Synthesis of copper oxide nanoparticles by chemical and biogenic methods: photocatalytic degradation and in vitro antioxidant activity. *Nanotechnol. Environ. Eng.*, **2020**, 5,14.
9. Alarifi, S., Ali, D., Al-Bishri. W. In vitro apoptotic and DNA damaging potential of nanobarium oxide. *Int. J. Nanomed.*, **2016**, 11, 249-257.
10. Renukadevi, R., Sundaram, R., Kaviyarasu. K. Barium Oxide nanoparticles with Robust Catalytic, Photocatalytic and Humidity Sensing Properties. *J. Nanostructures.*, **2020**, 10, 167-176.
11. E. Sundharam, A. Kingson, S. Jeevanraj, C. Chinnusamy. Effect of Ultrasonication on the Synthesis of Barium Oxide Nanoparticles. *J. Bionanosci.*, 2017, 11, 310-314.
12. Choudhary, R. V., Jha, V., Jana. P. Epoxidation of styrene by TBHP to styrene oxide using barium oxide as a highly active/selective and reusable solid catalyst. *Green Chem*, **2006**, 8 (8), 689-690,
13. Hamid, A., Khan, M., Hayat, A. et al., Probing the physio-chemical appraisal of green synthesized PbO nanoparticles in PbO-PVC nanocomposite polymer membranes", Spectrochimica Acta Part A: *Molecular and Biomolecular Spectroscopy*, **2020**, 235, 118303.
14. Dumkova, J., Smutna, T., Vrlikova, L. et al., "Variability in the Clearance of Lead Oxide Nanoparticles is Associated with Alteration of Specific Membrane Transporters", *ACS Nano*, **2020**, 14, 3096-3120.
15. Khalil, A., Ovais, M., Ullah, I., Ali, M., Jan, S.A., Shinwari, K.H., Mazaa, M., "Bioinspired synthesis of pure massicot phase lead oxide nanoparticles and assessment of their biocompatibility, cytotoxicity and in-vitro biological properties", *Arabian Journal of Chemistry*, **2020**, 13, 916-931.
16. Sonmez, M.S., Kumar, R.V., "Leaching of waste battery paste components. Part 1: Lead citrate synthesis from PbO and PbO_2", *Hydrometallurgy*, **2009**, 95, 53-60.
17. Sljuki, B., Banks, C.E., Crossley. A., Richard, G., Compton, R.G., "Lead (IV) oxide–graphite composite electrodes: Application to sensing of ammonia, nitrite and phenols", *Analytica Chimica Acta*, **2007**, 587, 240–246.
18. Yousefi, R., Zak, A.K., Jamali-Sheinic, F., Huangd, N.M., Basirun, W.J., Sookhakian, M., "Synthesis and characterization of single crystal PbO nanoparticles in a gelatin medium". *Ceramics International*, **2014**, 40, 11699-11703.
19. Sharma, D.; Mehta, B.R. Nanostructured TiO_2 thin films sensitized by CeO_2 as an inexpensive photoanode for enhanced photoactivity of water oxidation. *J. Alloys Compd.* **2018**, 749, 329–335.

20. Prajapati, K.D., Chouhan, K.J., Menaria, J., Tanwer, S.T., Bhardwaj, S. Fabrication and Characterization of Photocatalyst Pb3CdO7 for Degradation of Azure- A. *J. Environ. Sci. Pollut. Res.* **2024**, 10, 485–491.
21. Yin, D.; Zhao, F.; Zhang, L.; Zhang, X.; Liu, Y.; Zhang, T.; Wu, C.; Chen, D.; Chen, Z. Greatly enhanced photocatalytic activity of semiconductor CeO_2 by integrating with upconversion nanocrystals and graphene. *RSC Adv.* **2016**, 6, 103795–103802.
22. Aboutaleb, W.A.; El-Salamony, R.A. Effect of Fe_2O_3-CeO_2 nanocomposite synthesis method on the Congo red dye photodegradation under visible light irradiation. *Mater. Chem. Phys.* **2019**, 236, 121724.
23. Wang, B.; Zhu, B.; Yun, S.; Zhang, W.; Xia, C.; Afzal, M.; Cai, Y.; Liu, Y.; Wang, Y.; Wang, H. Fast ionic conduction in semiconductor $CeO_{2-\delta}$ electrolyte fuel cells. *NPG Asia Mater.* **2019**, 11, 51-59.
24. Murugan, R., Kashinath, L., Subash, R., Sakthivel, P., Byrappa, K., Rajendran, S., & Ravi, G. Pure and alkaline metal ion (Mg, Ca, Sr, Ba) doped cerium oxide nanostructures for photo degradation of methylene blue. *Materials Research Bulletin*, **2018**, 97, 319-325.
25. Shajahan, S., Arumugam, P., Rajendran, R., & Munusamy, A. P. Optimization and detailed stability study on Pb doped ceria nanocubes for enhanced photodegradation of several anionic and cationic organic pollutants. *Arabian Journal of Chemistry*, **2020**, 13(1), 1309-1322.
26. Magdalane, C. M., Kaviyarasu, K., Vijaya, J. J., Siddhardha, B., Jeyaraj, B., Kennedy, J., & Maaza, M. Evaluation on the heterostructured CeO_2/Y_2O_3 binary metal oxide nanocomposites for UV/Vis light induced photocatalytic degradation of Rhodamine-B dye for textile engineering application. Journal *of Alloys and Compounds*, **2017**, 727, 1324-1337.
27. Tabari, T., Tavakkoli, H., Zargaran, P., & Beiknejad, D. Fabrication of perovskite-type oxide $BaPbO_3$ nanoparticles and their efficiency in photodegradation of methylene blue. *South African Journal of Chemistry*, **2012**, 65(1), 239-244.
28. Karthik, R., Vinoth Kumar, J., Chen, S. M., Karuppiah, C., Cheng, Y. H., & Muthuraj, V. A study of electrocatalytic and photocatalytic activity of cerium molybdate nanocubes decorated graphene oxide for the sensing and degradation of antibiotic drug chloramphenicol. *ACS Applied Materials & Interfaces*, **2017**, 9(7), 6547-6559.
29. Garg, P., Khare, P., Shankar, R., & Tyagi, A. Sunlight-assisted electrochemical performance of vertical self-standing cerium-oxide nanoflakes decorated lead-oxide electrode for methylene blue removal. *Electrochimica Acta*, **2023**, 464, 142890.
30. Murugadoss, G., Ma, J., Ning, X., & Kumar, M. R. Selective metal ions doped CeO_2 nanoparticles for excellent photocatalytic activity under sun light and supercapacitor application. *Inorganic Chemistry Communications*, **2019**, 109, 107577.
31. Wu, J., Li, Q., Zhang, G., & Lv, Y. Synthesis, characterization, and photocatalysis of a rare-earth cerium/silver/zinc oxide inorganic nanocomposite. *Green Processing and Synthesis*, **2022**, 11(1), 503-511.
32. Mejia, V. Q., Hadechini, R. C., Barros, A. H., & De Ávila, Z. C. Synthesis and characterization of BaO nanorods using azadirachta indica (neem) leaf extract for environmental applications. *South African Journal of Chemical Engineering*, **2025**, 52, 189-199.
33. Basavanagoudra, H., Jangannanavar, V. D., Patil, M. K., Inamdar, S. R., & Goudar, K. M. Barium oxide nanorods: Catalyst concentration and surface defects' role in degrading methylene blue organic pollutant. *Chemical Physics Impact*, **2024**, 8, 100578.
34. Rahman, O., Ali, A., Husain, A., Khan, S. A., Tariq, M., Urooj, S., & Mihet-Popa, L. Investigation of CeO_2 nanoparticles on the performance enhancement of insulating oils. Heliyon, 2023, 9(9), 215-224
35. Çetinkaya, S., & Kütük, N. Rapid synthesis of PbO-NPs photocatalysts, investigation of methylene blue degradation kinetics. Gazi University Journal of Science, **2023**, 36(2), 511-527.
36. Magdalane, C. M., Kaviyarasu, K., Vijaya, J. J., Siddhardha, B., & Jeyaraj, B. Photocatalytic activity of binary metal oxide nanocomposites of CeO_2/CdO nanospheres: investigation of optical and antimicrobial activity. Journal of Photochemistry and Photobiology B: Biology, **2016**, 163, 77-86.

37. Manikanika, Chopra, L., & Kumar, R. Photocatalytic degradation efficiencies of ZnO nanoparticles and CeO_2 nanosheets synthesized via combustion method. *Bulletin of Materials Science*, **2023**, 46(3), 181.
38. Subhan, M. A., Ahmed, T., Uddin, N., Azad, A. K., & Begum, K. Synthesis, characterization, PL properties, photocatalytic and antibacterial activities of nano multi-metal oxide NiO· CeO_2· ZnO. Spectrochimica Acta Part A: *Molecular and Biomolecular Spectroscopy*, **2015**, 136, 824-831.
39. Naz, F., & Saeed, K. Synthesis of barium oxide nanoparticles and its novel application as a catalyst for the photodegradation of malachite green dye. *Applied Water Science*, **2022**, 12(6), 121.
40. Hussain, E., Majeed, I., Nadeem, M. A., Iqbal, A., Chen, Y., Choucair, M., & Nadeem, M. A. Remarkable effect of BaO on photocatalytic H_2 evolution from water splitting via TiO_2 (P25) supported palladium nanoparticles. Journal of Environmental Chemical Engineering, **2019**, 7(1), 102729.
41. Savunthari, K. V., Balaji, D., Sudheer, N., Bathwar, M., Rangasamy, M., Dhandabani, G. K., & Kong, K. V. Effective photocatalytic degradation of rhodamine-B over Zn-doped BaO_2 and SrO_2 composites under UV and sunlight irradiation. *RSC Sustainability*, **2023**, 1(6), 1511-1521.
42. Vaizogullar, A. I., Topkara, C., & Ugurlu, M. Ternary V-scheme Ag_2WO_4/BaO/NiO heterojunction photocatalysts: Very fast degradation process for congo red under UV-light irradiation. *ACS omega*, **2023**, 8(10), 9423-9433.
43. Islam, M. F., Oyshi, T. A., Hosen, N., Hassan, M. J., Shah, S. S., Rahaman, M., & Hasnat, M. A. Optimization of Electrocatalytic Chlorazol Yellow Degradation Using PbO_2 Nanostructure Immobilized on Stainless Steel Substrate. *Catalysts*, **2025**, 15(1), 34.
44. Bhachu, D. S., Sathasivam, S., Carmalt, C. J., & Parkin, I. P. PbO-modified TiO_2 thin films: a route to visible light photocatalysts. Langmuir, **2014**, 30(2), 624-630.
45. Pan, F., Raza, J., Khan, M., Ragab, A. H., Lei, T., Rafique, M. S., & Khan, I. Preparation and structural investigations of the composite containing lead oxide and graphite as reinforcements and its adsorptive and photocatalytic dye-degradation activity. Diamond and Related Materials, **2023**, 137, 110170.
46. Choi, J., Reddy, D. A., Islam, M. J., Ma, R., & Kim, T. K. Self-assembly of CeO_2 nanostructures/reduced graphene oxide composite aerogels for efficient photocatalytic degradation of organic pollutants in water. *Journal of Alloys and Compounds*, **2016**, 688, 527-536.
47. Channei, D., Inceesungvorn, B., Wetchakun, N., Ukritnukun, S., Nattestad, A., Chen, J., & Phanichphant, S. J. S. R. Photocatalytic degradation of methyl orange by CeO_2 and Fe–doped CeO2 films under visible light irradiation. *Scientific Reports*, **2014**, 4(1), 5757.
48. Rajendran, S., Khan, M. M., Gracia, F., Qin, J., Gupta, V. K., & Arumainathan, S. Ce^{3+}-ion-induced visible-light photocatalytic degradation and electrochemical activity of ZnO/CeO_2 nanocomposite. *Scientific reports*, **2016**, 6(1), 31641.
49. Raj, R. B., Umadevi, M., Parimaladevi, R., & Anuratha, M. (ZnO/BaO nanocomposites: a promising photocatalyst in degrading anionic and cationic dyes under UV and visible light and an efficient antibacterial agent. *Journal of Sol-Gel Science and Technology*, **2022**, 102(3), 628-636.
50. Borhade, A. V., Tope, D. R., & Uphade, B. K. An efficient photocatalytic degradation of methyl blue dye by using synthesised PbO nanoparticles. *Journal of chemistry*, **2012**, 9(2), 705-715.
51. Geldasa, F. T., Kebede, M. A., Shura, M. W., Andoshe, D. M., Tegegne, N. A., & Hone, F. G. Facile synthesis of different metals doped α-PbO nanoparticles for photocatalytic degradation of Methylene Blue dye. *Physica Scripta*, **2023**, 98(6), 065701.